



Anomalous transport on regular fracture networks: Impact of conductivity heterogeneity and mixing at fracture intersections

Peter K Kang, Marco Dentz, Tanguy Le Borgne, Ruben Juanes

► To cite this version:

Peter K Kang, Marco Dentz, Tanguy Le Borgne, Ruben Juanes. Anomalous transport on regular fracture networks: Impact of conductivity heterogeneity and mixing at fracture intersections. *Physical Review E: Statistical, Nonlinear, and Soft Matter Physics*, 2015, 92 (2), pp.022148. 10.1103/PhysRevE.92.022148 . insu-02442412

HAL Id: insu-02442412

<https://insu.hal.science/insu-02442412>

Submitted on 17 Feb 2021

HAL is a multi-disciplinary open access archive for the deposit and dissemination of scientific research documents, whether they are published or not. The documents may come from teaching and research institutions in France or abroad, or from public or private research centers.

L'archive ouverte pluridisciplinaire **HAL**, est destinée au dépôt et à la diffusion de documents scientifiques de niveau recherche, publiés ou non, émanant des établissements d'enseignement et de recherche français ou étrangers, des laboratoires publics ou privés.

This is the accepted manuscript made available via CHORUS. The article has been published as:

Anomalous transport on regular fracture networks: Impact of conductivity heterogeneity and mixing at fracture intersections

Peter K. Kang, Marco Dentz, Tanguy Le Borgne, and Ruben Juanes

Phys. Rev. E **92**, 022148 — Published 28 August 2015

DOI: [10.1103/PhysRevE.92.022148](https://doi.org/10.1103/PhysRevE.92.022148)

Anomalous transport on regular fracture networks: Impact of conductivity heterogeneity and mixing at fracture intersections

Peter K. Kang,^{1,2} Marco Dentz,³ Tanguy Le Borgne,⁴ and Ruben Juanes^{1,*}

¹*Massachusetts Institute of Technology, 77 Massachusetts Ave,
Cambridge, Massachusetts 02139, USA*

²*Korea Institute of Science and Technology, Seoul 136-791, Republic of Korea*

³*Institute of Environmental Assessment and Water Research (IDAEA),
Spanish National Research Council (CSIC), 08034 Barcelona, Spain*

⁴*Université de Rennes 1, CNRS, Geosciences Rennes, UMR 6118, Rennes, France*

(Dated: August 10, 2015)

Abstract

We investigate transport on regular fracture networks that are characterized by heterogeneity in hydraulic conductivity. We discuss the impact of conductivity heterogeneity and mixing within fracture intersections on particle spreading. We show the emergence of non-Fickian transport due to the interplay between the network conductivity heterogeneity and the degree of mixing at nodes. Specifically, lack of mixing at fracture intersections leads to subdiffusive scaling of transverse spreading but has negligible impact on longitudinal spreading. An increase in network conductivity heterogeneity enhances both longitudinal and transverse spreading and leads to non-Fickian transport in longitudinal direction. Based on the observed Lagrangian velocity statistics, we develop an effective stochastic model that incorporates the interplay between Lagrangian velocity correlation and velocity distribution. The model is parameterized with a few physical parameters and is able to capture the full particle transition dynamics.

PACS numbers: 05.60.Cd, 05.40.Fb, 05.10.Gg, 92.40.Kf

* juanes@mit.edu

I. INTRODUCTION

Understanding transport in network systems is of critical importance in many natural and engineered processes, including groundwater contamination and geothermal production in fractured geologic media [1, 2], disease spreading through river networks [3], engineered flows and medical applications in microfluidic devices [4], and urban traffic [5]. While particle spreading has traditionally been described using a Fickian framework, anomalous transport—characterized by the nonlinear scaling with time of the mean square displacement and the non-Gaussian scaling of solute distributions and fluxes—has been widely observed in porous and fractured media at various scales from pore [6–9] to column [10–12] to field scale [13–18]. The observation of anomalous transport is not limited to porous and fractured media, and has been observed in many different systems from diffusion of a molecule in a single cell to animal foraging patterns [19–21]. Predictability of the observed anomalous transport is essential because it controls the early arrival and the long residence time of particles [22–24]. This becomes especially important for environmental and human health related issues, such as radionuclide transport in the subsurface [25, 26], or water quality evolution in managed aquifer recharge systems [27–29].

Stochastic models that account for the observed non-Fickian transport behavior in porous and fractured media include continuous-time random walks (CTRW) [30–34], fractional advection-dispersion equations (fADE) [35, 36], multirate mass transfer (MRMT) [17, 37, 38], stochastic convective stream tube (SCST) models [39], and Boltzmann equation approaches [40]. All of these models have played an important role in advancing the understanding of transport through porous and fractured geologic media.

The CTRW formalism [41, 42] offers an attractive framework to describe and model anomalous transport through porous media and networks [30, 43, 44] because it allows incorporating essential flow heterogeneity properties directly through the Lagrangian velocity distribution. The CTRW approach successfully described average transport in quenched random environments from purely diffusive transport [e.g., 23] to biased diffusion [e.g., 45–48]. Most studies that employ the CTRW approach assume that successive particle jumps are independent of each other, therefore neglecting velocity correlation between jumps [49]. Indeed, a recent study showed that CTRW with independent transition times emerges as an exact macroscopic transport model when particle velocities are uncorrelated [48].

However, recent studies based on the analysis of Lagrangian particle trajectories demonstrates

conclusively that particle velocities in mass-conservative flow fields exhibit correlation along their trajectory [9, 40, 45, 50–53]. Mass conservation induces correlation in the Eulerian velocity field because fluxes must satisfy the divergence-free constraint at each intersection. This, in turn, induces correlation in the Lagrangian velocity along a particle trajectory. To take into account velocity correlation, Lagrangian models based on temporal [50, 54] and spatial [9, 40, 45, 51, 52] Markovian processes have recently been proposed. These models successfully capture many important aspects of the particle transport behavior. The importance of velocity correlation has also been recently shown for a field-scale tracer transport experiment [18].

Following the work by Le Borgne *et al.* [45], the spatial Markov model for particle velocities at Darcy-scale has been recently extended to describe multidimensional transport at both pore- and network-scale [9, 51]. The model captures multidimensional features of transport via a multidimensional velocity transition matrix. In these approaches, the transition matrices are constructed utilizing Lagrangian velocity information obtained from direct numerical simulations. Therefore, for an effective parameterization in terms of the medium geometry and the statistical characteristics of the Eulerian velocity, a model for the velocity transition process is crucial. Furthermore, it is well known that the mixing at fracture intersections and fracture conductivity distribution has major impact on transport properties [55–58]. However, the impact of the interplay between the network conductivity heterogeneity and the mixing dynamics at fracture intersections on anomalous transport, and the ability of spatial Markov models to capture it, is still an open question.

The paper proceeds as follows. In the next section, we present the heterogeneous fracture network, the flow and transport equations and details of the different mixing rules at fracture intersections. In Section III, we investigate the emergence of anomalous transport by direct Monte Carlo simulations of flow and particle transport. In Section IV, we analyze the statistics of the Lagrangian particle velocities measured equidistantly along the particle trajectories to gain insight into the effective particle dynamics and elucidate the origins of the observed anomalous behavior. In Section V, we develop a spatial Markov model that is characterized by the probability density function (PDF) of Lagrangian velocities and their transition PDF, which are derived from the Monte Carlo simulations. The resulting correlated CTRW model is in excellent agreement with Monte Carlo simulations. In Section VI, we then present a physics-based spatial Markov model for the velocity transitions that is characterized by only a few parameters, which are directly related to the properties of the conductivity heterogeneity and the mixing rules at fracture intersections. The predictive capabilities of this model are demonstrated by comparison to the direct Monte Carlo

simulations. In Section VII, we summarize the main findings and conclusions.

II. FLOW AND TRANSPORT THROUGH REGULAR FRACTURE NETWORKS

We study a regular fracture network consisting of two sets of parallel, equidistant fractures oriented at an angle of $\pm\alpha$ with the x -axis. The distance between the neighboring nodes is l (Figure 1). Flow through the network is modeled by Darcy's law [59] for the fluid flux u_{ij} between nodes i and j , $u_{ij} = -K_{ij}(\Phi_j - \Phi_i)/l$, where Φ_i and Φ_j are the hydraulic heads at nodes i and j , and $K_{ij} > 0$ is the hydraulic conductivity of the link between the two nodes. Imposing mass conservation at each node i , $\sum_j u_{ij} = 0$ (the summation is over nearest-neighbor nodes), leads to a linear system of equations, which is solved for the hydraulic heads at the nodes. The fluid flux through a link from node i to j is termed incoming for node i if $u_{ij} < 0$, and outgoing if $u_{ij} > 0$. We denote by \mathbf{e}_{ij} the unit vector in the direction of the link connecting nodes i and j . A realization of the random regular network is generated by assigning independent and identically distributed random conductivities to each link. Therefore, the K_{ij} values in different links are uncorrelated. The set of all realizations of the quenched random network generated in this way forms a statistical ensemble that is stationary and ergodic. We assign a lognormal distribution of K values. We study the impact of conductivity heterogeneity on transport by varying the variance of $\ln(K)$. The use of this particular distribution is motivated by the fact that conductivity values in many natural media can be described by a lognormal law [60].

We study a uniform flow setting characterized by constant mean flow in the positive x -direction, by imposing no-flow conditions at the top and bottom boundaries of the network, and fixed hydraulic head at the left ($\Phi = 1$) and right ($\Phi = 0$) boundaries. Thus, the mean flow velocity is given by $\bar{u} = K_g$ where $K_g = \exp(\overline{\ln K})$ is the geometric mean conductivity. The overbar in the following denotes the ensemble average over all network realizations. Even though the underlying conductivity field is uncorrelated, the mass conservation constraint together with heterogeneity leads to the formation of preferential flow paths with increasing network heterogeneity. (Figure 2).

Once the fluxes at the links have been determined, we simulate transport of a passive tracer by particle tracking. We neglect the longitudinal diffusion along links, and thus particles are advected with the mean flow velocity between nodes. Here we assume that Darcy's law is valid in each link, which means we assume that the links are filled with a porous medium characterized by variable conductivity, but constant porosity. This is motivated also by the fact that the variability

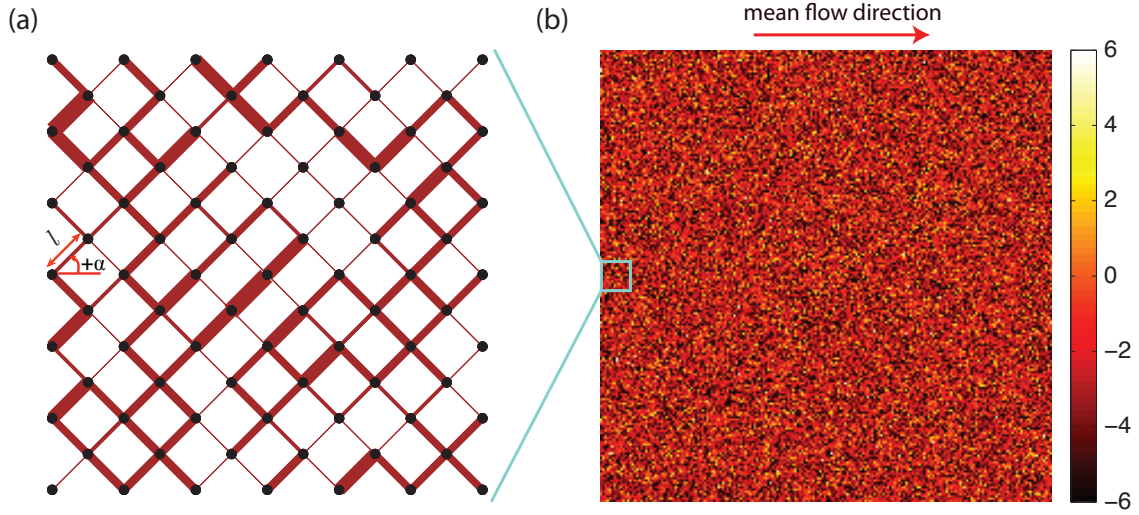


FIG. 1. (a) Schematic of the fracture network studied here, with two sets of links with orientation $\pm\alpha = \pm\pi/4$ and uniform spacing l . The conductivity values are reflected in the link thickness. We study log-normal conductivity distributions with three different conductivity variance values: $\sigma_{\ln K}^2 = 0.1, 1, 5$. (b) Map of the spatially uncorrelated conductivity field with $\sigma_{\ln K}^2 = 5$ shown in a log-scale color scheme. No flow boundary conditions on the top and bottom and constant hydraulic head on the left and right boundaries ensure a uniform mean flow.

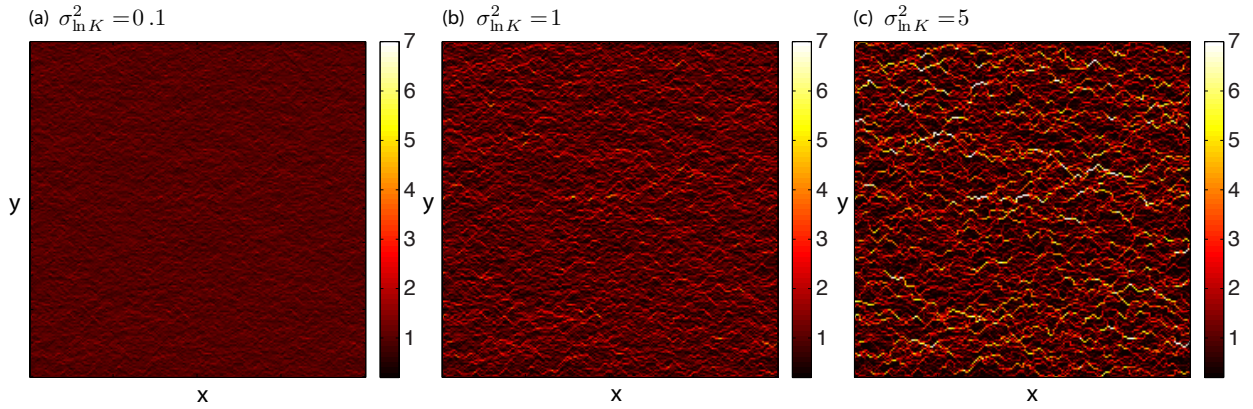


FIG. 2. (a) Normalized flow field ($|u_{ij}|/\bar{u}$) for log-normal conductivity distribution with variance 0.1. (b) Normalized flow field for log-normal conductivity distribution with variance 1. (c) Normalized flow field for log-normal conductivity distribution with variance 5. Even though the underlying conductivity field is uncorrelated, the combined effect of network heterogeneity and the mass conservation constraint at nodes leads to a correlated flow field with preferential flow paths.

in porosity is typically much smaller than the conductivity variability [59, 61]. When particles arrive at nodes, they follow either complete mixing or streamline routing (no mixing) rule [56–58]. Complete mixing assumes that Péclet numbers at nodes are small enough that particles are well mixed within the node. Thus, the link through which the particle exits a node is chosen randomly with flux-weighted probability. Streamline routing assumes that Péclet numbers at nodes are large enough that particles essentially follow the streamlines and do not transition between streamlines. The complete mixing and streamline routing rules are two end members. In general, the local Péclet number and the intersection geometry determine the strength of mixing at nodes, which is in between these two end members.

In Figure 3 we illustrate the fundamental difference between the two mixing rules. When the two incoming and the two outgoing links have equal fluxes, the particles from the incoming link partition equally into the two outgoing links for the complete mixing rule. However, for the streamline routing case, all particles transit to the adjacent link. Therefore, we anticipate that the degree of mixing at the nodes will lead to a dramatically different global spreading behavior.

For complete mixing, the particle transfer probabilities p_{ij} from node i to node j are given by

$$p_{ij} = \frac{|u_{ij}|}{\sum_k |u_{ik}|}, \quad (1)$$

where the summation is over outgoing links only, and $p_{ij} = 0$ for incoming links. Particle transitions are determined only by the outgoing flux distribution. Equation (1) applies to both complete mixing and streamline routing rules for nodes with three outgoing fluxes and one incoming. However, for nodes with two outgoing fluxes, streamline routing implies the transfer probabilities

$$p_{\text{adj}} = \begin{cases} 1, & u_{\text{adj}} > u_{\text{in}} \\ \frac{u_{\text{adj}}}{u_{\text{in}}}, & u_{\text{adj}} < u_{\text{in}} \end{cases} \quad p_{\text{opp}} = \begin{cases} 0, & u_{\text{adj}} > u_{\text{in}} \\ \frac{u_{\text{in}} - u_{\text{adj}}}{u_{\text{in}}}, & u_{\text{adj}} < u_{\text{in}}, \end{cases} \quad (2)$$

where p_{adj} is the probability of a particle transitioning to an adjacent link and p_{opp} is the probability of a particle transitioning to an opposite link (Figure 3).

The Langevin equations describing particle movements in space and time are

$$\mathbf{x}_{n+1} = \mathbf{x}_n + l \frac{\mathbf{v}(\mathbf{x}_n)}{|\mathbf{v}(\mathbf{x}_n)|}, \quad t_{n+1} = t_n + \frac{l}{|\mathbf{v}(\mathbf{x}_n)|}. \quad (3)$$

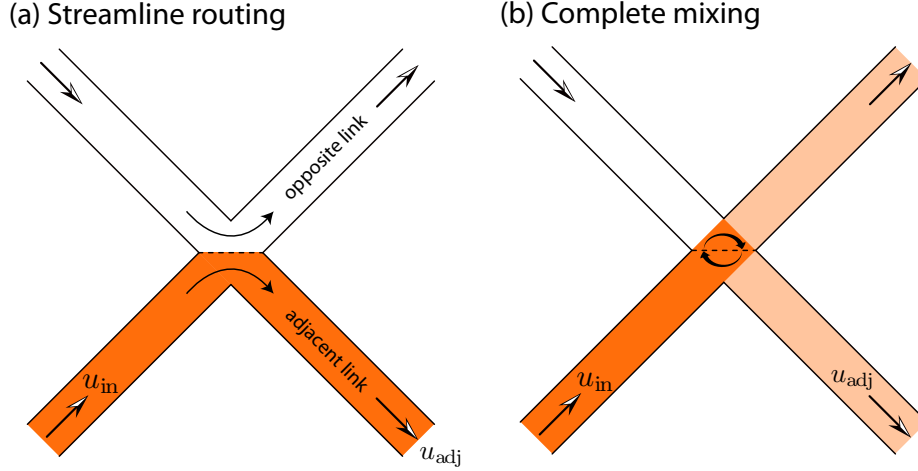


FIG. 3. Schematic for the two different mixing rules for the case in which nodes at the two incoming and the two outgoing links have equal fluxes. (a) The streamline routing rule makes all the particles transit to the adjacent link because particles cannot switch between streamlines. (b) The complete mixing rule makes half of the particles move upward and the other half downward, following flux-weighted probabilities.

where \mathbf{x}_n is the position of the n th node visited by the tracer particle, and t_n is the time at which the tracer particle arrives the n th node. The transition velocity is equal to $\mathbf{v}(\mathbf{x}_n) = u_{ij}\mathbf{e}_{ij}$ with the transition probability p_{ij} following either Equation (1) or (2) depending on the mixing rule. The velocity vector \mathbf{v} in the following is expressed in (ν, θ) coordinates, in which $\nu = |v| \cos(\varphi) / |\cos(\varphi)|$ is the velocity along a link with $\varphi = \arccos(v_x/|v|)$ and $\theta = \sin(\varphi) / |\sin(\varphi)|$, so that $\mathbf{v} = [\nu \cos(\alpha), |\nu| \theta \sin(\alpha)]^T$. Superscript T denotes the transpose. Note that φ can only assume values in $\{-\alpha, \alpha, \pi - \alpha, \pi + \alpha\}$. In short, ν determines the velocity magnitude and longitudinal directionality and θ determines the transverse velocity directionality.

The system of discrete Langevin equations (3) describes coarse-grained particle transport for a single realization of the quenched random network. Particle velocities and thus transition times depend on the particle position. The particle position at time t is $\mathbf{x}(t) = \mathbf{x}_{n_t}$, where n_t denotes the number of steps needed to reach time t . The particle density in a single realization is $P(\mathbf{x}, t) = \langle \delta(\mathbf{x} - \mathbf{x}_{n_t}) \rangle$, where the angular brackets denote the noise average over all particles. We solve transport in a single disorder realization by particle tracking based on Equation (3) with the point-wise initial condition $\mathbf{x}_0 = \mathbf{0}$ and $t_0 = 0$. \mathbf{x}_0 is located at the center of the left boundary (marked by red star in Figure 4). As shown in Figure 4, both network heterogeneity and mixing rule at nodes have significant impact on particle spreading. An increase in network heterogeneity leads

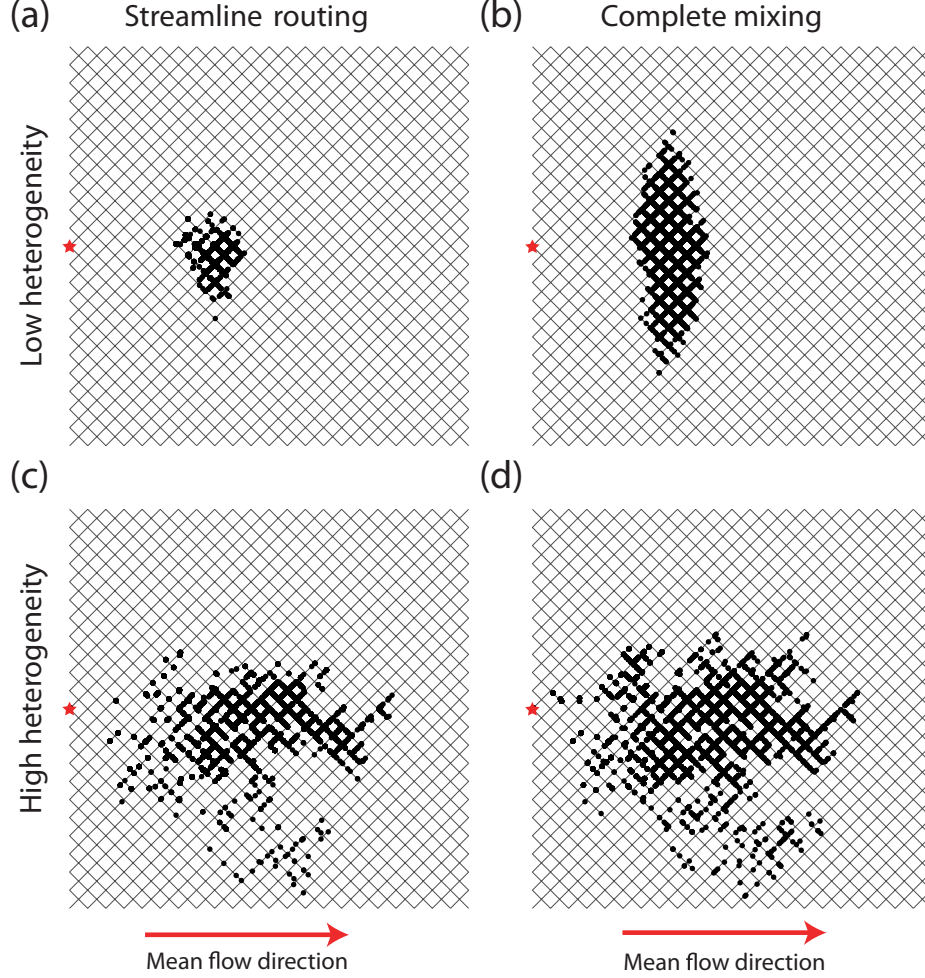


FIG. 4. Particle distribution at $t = 15\bar{t}_l$ for a given realization after the instantaneous release of particles at the origin (red star). \bar{t}_l is the mean advective time along one link. (a) Low heterogeneity ($\sigma_{\ln K}^2 = 0.1$) with streamline routing at nodes. (b) Low heterogeneity ($\sigma_{\ln K}^2 = 0.1$) with complete mixing at nodes. (c) High heterogeneity ($\sigma_{\ln K}^2 = 5$) with streamline routing at nodes. (d) High heterogeneity ($\sigma_{\ln K}^2 = 5$) with complete mixing at nodes. For low heterogeneity, complete mixing significantly enhances transverse spreading. An increase in heterogeneity significantly enhances longitudinal spreading.

156 to an increase in particle spreading in both transverse and longitudinal directions. The impact
 157 of the mixing rule has a significant impact on transverse mixing, especially for networks with
 158 low heterogeneity. Complete mixing at nodes significantly enhances transverse spreading while
 159 longitudinal spreading is much less sensitive to the mixing rule.

160 III. AVERAGE SOLUTE SPREADING BEHAVIOR

161 We study the average solute spreading behavior for three different conductivity variances and
 162 the two mixing rules described above. We obtain the mean particle density, $\overline{P}(\mathbf{x}, t)$, by ensemble
 163 averaging over multiple realizations,

$$\overline{P}(\mathbf{x}, t) = \overline{\langle \delta(\mathbf{x} - \mathbf{x}_{nt}) \rangle}, \quad (4)$$

164 where the overbar denotes the ensemble average over all realizations. We run Monte Carlo
 165 particle tracking simulations for 10^2 realizations for each combination of conductivity variance
 166 and mixing rule. We consider three different $\ln(K)$ variances, $\sigma_{\ln K}^2 = 0.1, 1, 5$. The domain size
 167 is $100\sqrt{2}l \times 100\sqrt{2}l$ with 20, 201 nodes. In each realization, we release 10^4 particles at the origin
 168 (\mathbf{x}_0 , marked by a red star in Figure 4). The average particle spreading behavior is studied in terms
 169 of the mean square displacement (MSD) of average particle density, $\overline{P}(\mathbf{x}, t)$. For the longitudinal
 170 direction (x), the MSD is given by $\sigma_x^2(t) = \overline{\langle [x(t) - \langle x(t) \rangle]^2 \rangle}$ where $\langle \cdot \rangle$ denotes the average over
 171 all particles for a given realization. The same definition is applied to compute the transverse MSD,
 172 σ_y^2 .

173 In Figure 5, we show the time evolution of the longitudinal and transverse MSDs. In both
 174 directions, spreading shows a ballistic regime ($\sim t^2$) at early times, which then transitions to a
 175 different preasymptotic scaling in an intermediate regime. The transition occurs approximately at
 176 the mean advective time over one link, \overline{t}_l .

177 The Monte Carlo simulations show that, in the intermediate regime, the *longitudinal* MSD
 178 increases linearly with time for weak conductivity heterogeneity [Figure 5(a)], and faster than
 179 linearly (i.e., superdiffusively) for intermediate to strong heterogeneity [Figure 5(c)(e)]. An in-
 180 crease in $\ln(K)$ variance significantly increases the longitudinal MSD and induces a change in its
 181 temporal scaling. The Monte Carlo simulations also show that there is no noticeable difference
 182 between complete mixing and streamline routing cases on longitudinal MSD. This indicates that
 183 the network heterogeneity dictates the longitudinal spreading in regular networks.

184 The *transverse* MSD evolves linearly in time for complete mixing, and slower than linearly
 185 with time (i.e., subdiffusively) for streamline routing [Figure 5(b)(d)(f)]. In contrast with the lon-
 186 gitudinal MSD, the transverse MSD exhibits a strong dependence on the mixing rule at fracture
 187 intersections. For low heterogeneity, complete mixing induces a significantly higher transverse

MSD than streamline routing. This difference, however, decreases as the network heterogeneity increases. For streamline routing, the network heterogeneity is the main driver for transitions in the transverse direction, and thus we clearly observe that transverse spreading increases as heterogeneity increases. The complete mixing rule, on the other hand, already maximizes transitions in the transverse direction so that an increase in heterogeneity has no significant impact.

In order to obtain complementary information on the spreading process, we also consider the first passage time distribution (FPTD) of particles at a control plane $x = \chi$, which acts like an absorbing barrier. The FPTD or, in other words, solute breakthrough curve, is obtained from the individual particle arrival times $\tau_a = \inf(t_n | |x_n - x_0| > \chi)$ as

$$f_\chi(\tau) = \overline{\langle \delta(\tau - \tau_a) \rangle}. \quad (5)$$

It provides an alternative measure of longitudinal spreading. Figure 6 illustrates FPTDs for different conductivity heterogeneities and mixing rules. Conductivity heterogeneity has a clear impact on the FPTD by enhancing longitudinal spreading. This is so because stronger conductivity heterogeneity leads to broader particle transition time distribution, which in turn leads to enhanced longitudinal spreading. The mixing rule, in contrast, has a negligible impact on FPTDs, and only influences transverse spreading. To understand this behavior and further quantify transverse spreading, we define the distribution of the transverse exit locations at a control plane $x = \chi$ as

$$f_\chi(\omega) = \overline{\langle \delta(\omega - y_e) \rangle}. \quad (6)$$

where y_e is the transverse location of a particle at the control plane at $x = \chi$. The impact of the mixing rule on transverse spreading is clearly visible in Figure 7, which compares $f_\chi(\omega)$ for different values of $\sigma_{\ln K}^2$ and different mixing rules. For small $\ln(K)$ variances, the mixing rule has a major impact on transverse spreading, which here is manifested by the width of the transverse particle distribution. The difference between the two mixing rules decreases as $\sigma_{\ln K}^2$ increases.

In summary, conductivity heterogeneity impacts both longitudinal and transverse spreading, whereas the mixing rule mainly impacts transverse spreading. We now analyze the Lagrangian particle statistics to understand the underlying physical mechanisms that lead to the observed anomalous particle spreading.

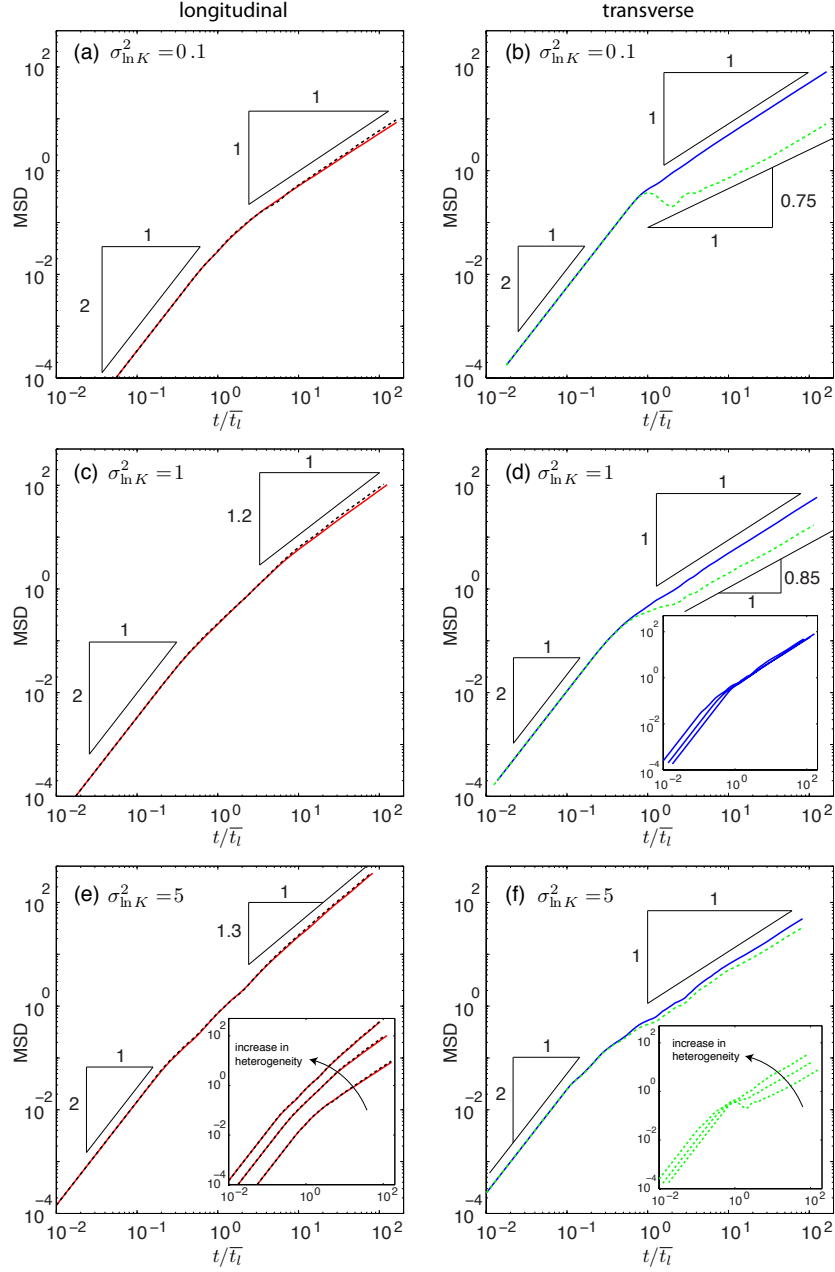


FIG. 5. Time evolution of MSDs for complete mixing (solid line) and streamline routing (dashed line). (a) Longitudinal MSD for $\sigma_{\ln K}^2 = 0.1$. (b) Transverse MSD for $\sigma_{\ln K}^2 = 0.1$. (c) Longitudinal MSD for $\sigma_{\ln K}^2 = 1$. (d) Transverse MSD for $\sigma_{\ln K}^2 = 1$. Inset: Change in the time evolution of transverse MSD for complete mixing with increasing variance. (e) Longitudinal MSD with $\sigma_{\ln K}^2 = 5$. Inset: Change in the time evolution of longitudinal MSD for complete mixing with increasing variance. (f) Transverse MSD with $\sigma_{\ln K}^2 = 5$. Inset: Change in the time evolution of transverse MSD for streamline routing with increasing conductivity variance.

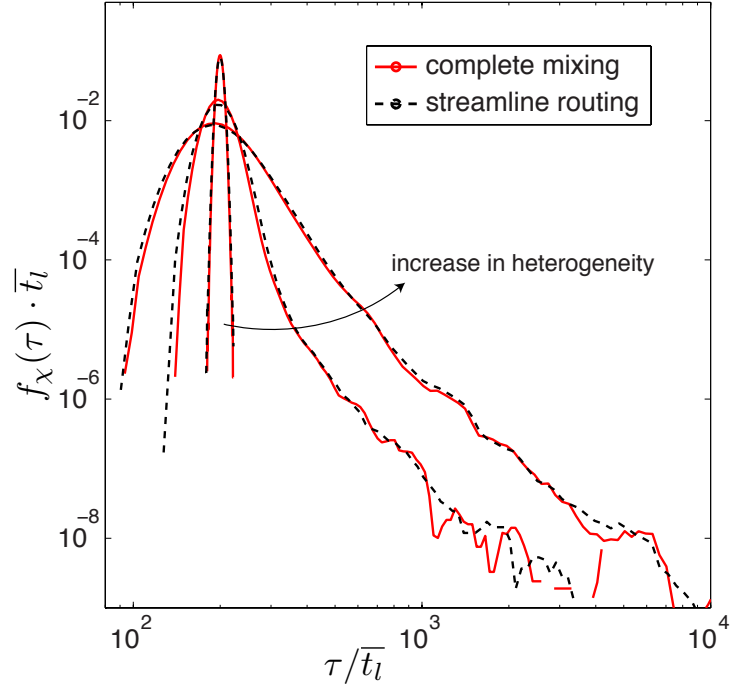


FIG. 6. First passage time distribution $f_{\chi}(\tau)$ for $\sigma_{\ln K}^2 = 0.1, 1, 5$ and different mixing rules. Conductivity heterogeneity has a major impact on particle breakthrough curves, in contrast to the mixing rules.

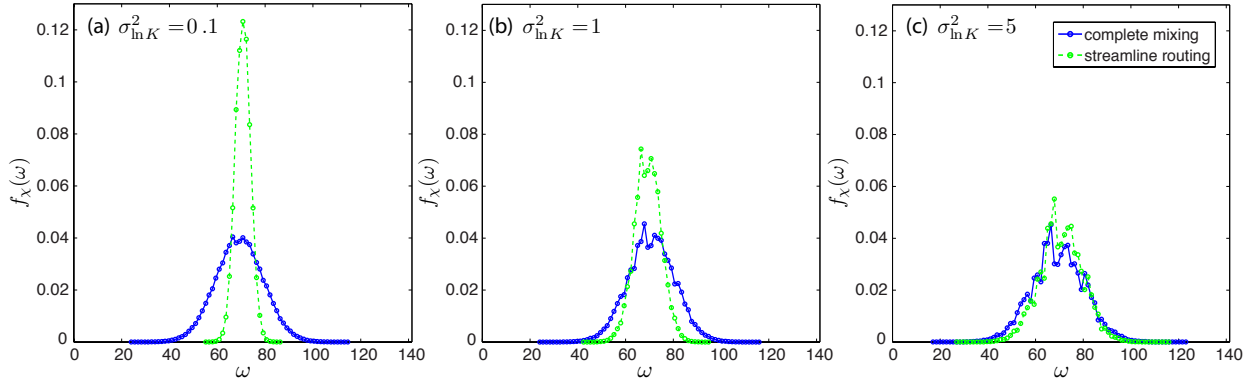


FIG. 7. Transverse breakthrough positions distribution (TBPd) at the outlet plane. Comparison between the two different mixing rules for (a) $\sigma_{\ln K}^2 = 0.1$, (b) $\sigma_{\ln K}^2 = 1$ and (c) $\sigma_{\ln K}^2 = 5$. The impact of the mixing rule on transverse spreading diminishes as the network heterogeneity increases.

IV. LAGRANGIAN VELOCITY DISTRIBUTION AND VELOCITY CORRELATION STRUCTURE

The mechanisms leading to anomalous transport can be understood through the analysis of the statistics of Lagrangian particle velocities [9, 18, 45, 50–52]. We consider here the particle velocities at fixed positions along their trajectories. The Lagrangian velocity $\mathbf{v}_L(s_n)$ at a distance $s_n = nl$ along the particle trajectory is given by $\mathbf{v}_L(s_n) = \mathbf{v}(\mathbf{x}_n)$ with \mathbf{x}_n the particle position in the network after n steps. Its absolute value, i.e., the streamwise velocity is $v_L(s_n) = |\mathbf{v}(s_n)|$. We now analyze the Lagrangian velocity correlation structure, and the PDF of transition times between nodes along trajectories, which is given by $\tau_n = l/v_L(s_n)$.

This is in contrast with the classical Lagrangian viewpoint, which considers particle velocities at fixed times along trajectories, $\mathbf{u}_L(t) = \mathbf{v}(\mathbf{x}_{n_t})$ where n_t is the number of steps needed to arrive at time t through the time process in Equation (3). The distance covered along the streamline up to time t then is given by $s(t) = n_t l$, and the streamwise Lagrangian velocity is given by $u_L(t) = |\mathbf{v}(\mathbf{x}_{n_t})|$.

We compute the steady-state transition time and velocity distributions along streamlines, $\psi_\tau(t)$ and $p_L(v)$, respectively, through sampling the transition times and velocities along all particle trajectories and among network realizations. Figure 8(a) illustrates the PDF of transition times and velocities for different $\ln(K)$ variances. As $\sigma_{\ln K}^2$ increases, the transition time and velocity PDFs become broader. The transition time follows closely a truncated power-law distribution. Both velocity and transition time distributions did not show noticeable difference between complete mixing [Figure 8(a)] and streamline routing [not shown].

A broad transition time distribution is known to be a source of anomalous transport behavior, and a key input parameter for the CTRW framework [31, 43]. For example, an optimal distribution of transition times may be inferred by interpreting first-passage time distributions [49]. However, the transition time distribution alone does not have information on the spatial velocity correlation structure, which may be an important factor that controls anomalous transport behavior [9, 18, 45, 47, 51, 52]. To analyze the Lagrangian correlation structure, we compute the velocity autocorrelation function.

The autocorrelation function for a given lag $\Delta s = s - s'$ is defined as

$$\chi_s(s', s' + \Delta s) = \frac{\langle [v_L(s' + \Delta s) - \langle v_L(s' + \Delta s) \rangle][v_L(s') - \langle v_L(s') \rangle] \rangle}{\sigma_v(s' + \Delta s)\sigma_v(s')}, \quad (7)$$

where $\sigma_v^2(s)$ is the variance of the Lagrangian velocity at a travel distance s . It depends in general on the starting position depending on the distribution of initial particle velocities. Here, particles are injected at the origin within each realization. This implies that particles sample uniformly from the heterogeneous flow velocity. The stationary streamwise velocity distribution, in contrast, is obtained by spatial sampling along particle pathlines. As a consequence, here, the correlation function depends on the starting point s' . However, with increasing streamwise distance from the injection point, the autocorrelation becomes stationary. Thus, we define the stationary autocorrelation function $\chi_s(s - s')$ by averaging over Eq. (7) as

$$\chi_s(\Delta s) = \frac{1}{a} \int_0^a ds_1 \chi_s(s_1, s_1 + \Delta s), \quad (8)$$

241 where we use $a = 100\ell$.

242 For comparison, we also consider the correlation of Lagrangian velocities $u_L(t)$ sampled *in*
243 *time* along particle trajectories. It is defined analogously as

$$\chi_t(t - t') = \frac{1}{T} \int_0^T dt' \frac{\overline{[u_L(t') - \langle u_L(t') \rangle][u_L(t' + \Delta t) - \langle u_L(t' + \Delta t) \rangle]}}{\sigma_u(t' + \Delta t)\sigma_u(t')}, \quad (9)$$

244 where $\Delta t = t - t'$. Figure 8(b) illustrates the Lagrangian autocorrelation function $\chi_s(s)$ for
245 different $\ln(K)$ variances with a complete mixing rule. The correlation length scale ℓ_c is defined
246 by

$$\ell_c = \int_0^\infty ds \chi_s(s). \quad (10)$$

247 The correlation function $\chi_s(s)$ is well represented by an exponential that is characterized by ℓ_c .
248 Under the complete mixing rule, we find that ℓ_c increases as the network heterogeneity increases,
249 indicating an increase in velocity correlation ($\ell_c = 1.01, 1.34, 2.13$ for $\sigma_{\ln K}^2 = 0.1, 1, 5$, respec-
250 tively). This is mainly due to the emergence of preferential flow paths, as shown in Figure 2. The
251 inset in Figure 8(b) compares the correlation functions $\chi_s(s)$ and $\chi_t(t)$ plotted against distance
252 normalized by the link length l and time normalized by the mean advection time across a link, for
253 $\sigma_{\ln K}^2 = 5$. Velocity correlation in time is significantly stronger than velocity correlation in space,
254 and closely follows a power law with slope 0.7. The reason for this slow decay in the temporal

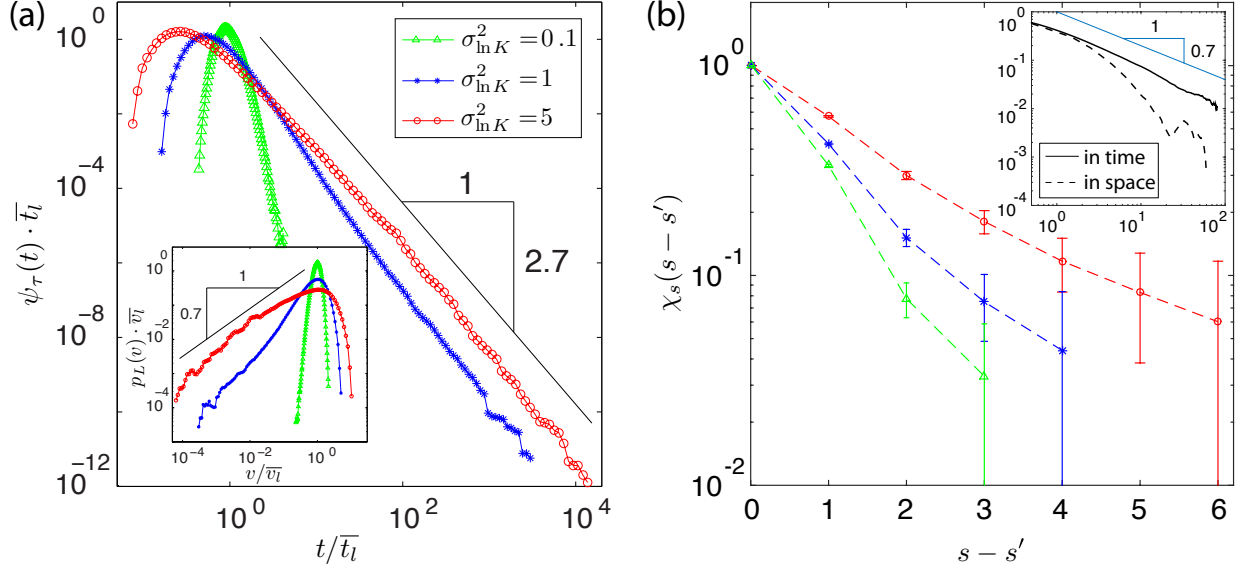


FIG. 8. (a) Lagrangian transition time distributions for $\sigma_{\ln K}^2 = 0.1, 1, 5$ and complete mixing at the nodes. Inset: Lagrangian velocity distributions for the three different values of $\sigma_{\ln K}^2$. As the network conductivity becomes more heterogeneous, both the transition time distribution and the velocity distribution become broader. (b) Velocity autocorrelation function in space. Error bars represent the coefficient of variation. An increase in network heterogeneity leads to stronger correlation. Inset: Comparison between the velocity autocorrelation in space and in time for $\sigma_{\ln K}^2 = 5$. Velocity autocorrelation in time is normalized with the mean advective time along one link, and velocity autocorrelation in space is normalized with the link length.

velocity correlation structure is the contribution from particles at stagnation zones (links with very small velocity values).

To further analyze and characterize the (spatial) Lagrangian velocity series $\{v(s_n)\}$, we compute the velocity transition matrix. To this end, we determine the transition probability density to encounter a velocity \mathbf{v} after $n + m$ steps given that the particle velocity was \mathbf{v}' after n steps, which in the variables (ν, θ) reads as

$$r_m(\nu, \theta | \nu', \theta') = \overline{\langle \delta[\nu - \nu(\mathbf{x}_{n+m})] \delta_{\theta, \theta(\mathbf{x}_{n+m})} \rangle} \Big|_{\nu(\mathbf{x}_n) = \nu', \theta(\mathbf{x}_n) = \theta'}. \quad (11)$$

To evaluate the transition probability numerically, the particle velocity distribution is discretized into classes, $\nu \in \bigcup_{j=1}^N (\nu_j, \nu_{j+1}]$, with $N = 100$. We may discretize velocity equiprobably in linear or logarithmic scale. The logarithmic scale provides a better discretization for low velocities, which have a decisive role for the occurrence of anomalous transport because they determine

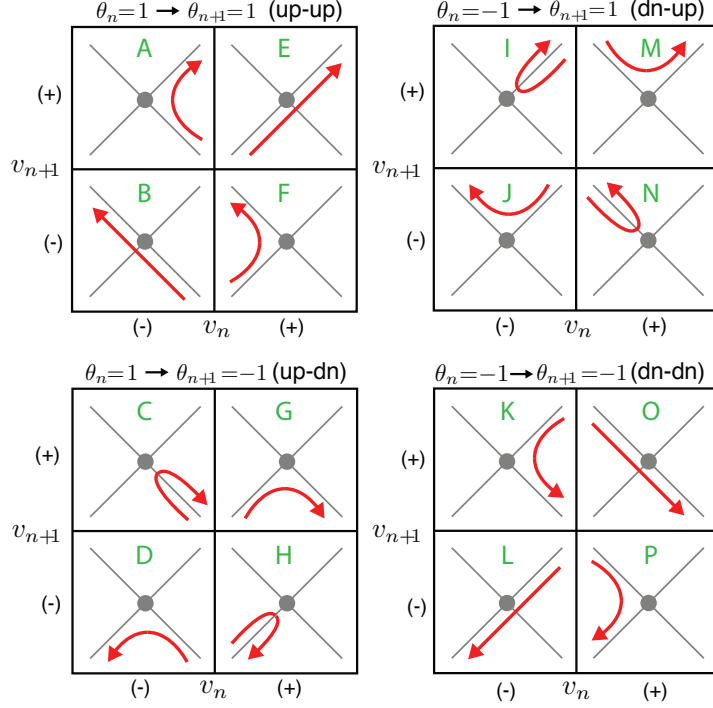


FIG. 9. Schematic of the velocity transition matrix for $d = 2$ dimensional networks. The transition matrix considers all 16 possible transitions to capture the full particle transport dynamics. The matrix has information about the one-step correlation, directionality and velocity heterogeneity.

the tailing behavior in FPTDs and spatial profiles. High velocities may be represented by only a few characteristic values. We define the transition probability matrix

$$T_m(i, \theta | j, \theta') = \frac{\int_{\nu_i}^{\nu_{i+1}} d\nu \int_{\nu_j}^{\nu_{j+1}} d\nu' r_m(\nu, \theta | \nu', \theta') p(\nu', \theta')}{\int_{\nu_j}^{\nu_{j+1}} d\nu' p(\nu', \theta')}, \quad (12)$$

where $p(\nu, \theta) = \overline{\langle \delta[\nu - \nu(\mathbf{x}_n)] \delta_{\theta, \theta(\mathbf{x}_n)} \rangle}$ is the joint single point PDF of ν and θ .

The transition matrices can be obtained numerically from the ensemble of particle trajectories. In $d = 2$ dimensional networks, there are sixteen possible transitions, which are described by a multi-dimensional transition matrix (Figure 9). We measure particle velocity transitions from link to link (equidistance in space) and populate the respective entries in the transition matrix. The one-step transition matrices $T_1(i, \theta | j, \theta')$ for two different heterogeneity distributions and mixing rules with equiprobable binning are shown in Figures 10 and 11. For small heterogeneity ($\sigma_{\ln K}^2 = 0.1$, Figure 10), the difference in the transition matrix for complete mixing and streamline routing at nodes is significant. This difference diminishes as heterogeneity increases ($\sigma_{\ln K}^2 = 5$, Figure 11).

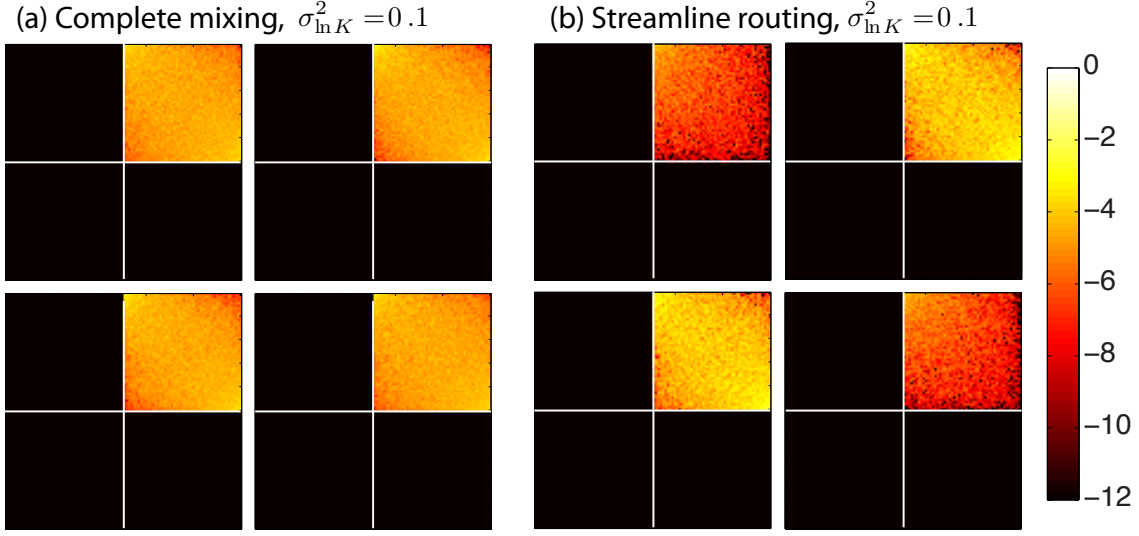


FIG. 10. (a) Velocity transition matrix with linear equiprobable binning for $\sigma_{\ln K}^2 = 0.1$ and *complete mixing* at nodes. Out of 16 transitions, only the four that have forward-forward movement in longitudinal direction (E, M, G, O) are possible. Note that the probability for each possible transition is almost identical. (b) Velocity transition matrix with linear equiprobable binning for $\sigma_{\ln K}^2 = 0.1$ with *streamline routing*. Again, only the four transitions that have forward-forward movement in longitudinal direction (E, M, G, O) are possible. Also, note that the probability for M and G transitions (0.89) is significantly higher than E and O transitions (0.11).

Network heterogeneity also exerts a significant impact on the particle transition matrix: as conductivity distribution becomes more heterogeneous, the probability of transitions with flow reversal (negative x -direction) increases. Higher probability values along the diagonal of the transition matrix reflect the spatial velocity correlation. Similarly, the upper triangular and lower triangular matrices in the transitions with backward movement (A, F, K, P) indicate that the velocity magnitude is typically smaller for backward movements than for forward movements.

The clear differences between transition time matrices for different mixing rules indicate the importance of taking the directionality of particle transport into account. Nonlocal theories of transport, including CTRW, are often invoked to explain the observation that the first passage time distribution (FPTD) is broad-ranged [16–18, 43]. Early arrival and slow decay of the FPTD is also observed in our model system. To develop a predictive transport model for the observed average particle density $\bar{P}(\mathbf{x}, t)$, we study average particle movements from a CTRW point of view that incorporates the velocity correlation and velocity distribution (heterogeneity). This approach

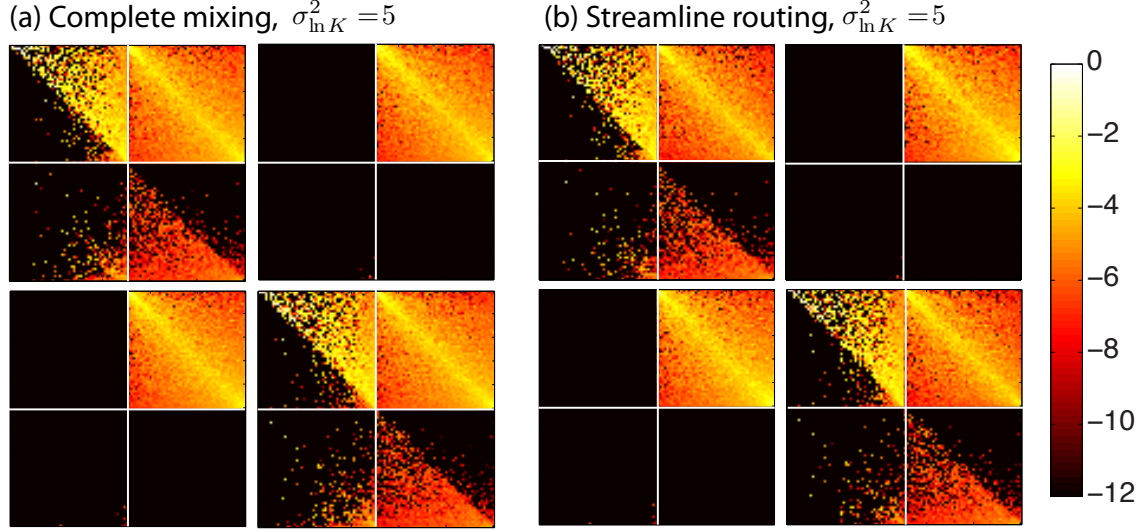


FIG. 11. (a) Velocity transition matrix with linear equiprobable binning for $\sigma_{\ln K}^2 = 5$ and *complete mixing* at the nodes. Due to strong heterogeneity, 12 different transitions, including backward movements, are possible. Also, note that up-up and down-down transitions (A, F, K, P) have triangular matrices. This indicates that velocity magnitudes mostly increase when a particle changes direction from $-x$ direction to $+x$ direction and vice versa. (b) Velocity transition matrix with linear equiprobable binning for $\sigma_{\ln K}^2 = 5$ and *streamline routing*. Since strong heterogeneity dictates particle transitions, there is no significant difference between complete mixing and streamline routing.

has been recently proposed for lattice fracture networks based on the finding that the series of particle velocities $\{\mathbf{v}_L(s_n)\}$ sampled spatially along a particle trajectory form in fact a Markov process [51].

V. SPATIAL MARKOV MODEL: A CORRELATED CONTINUOUS TIME RANDOM WALK

The series of Lagrangian velocities $\{\mathbf{v}_L(s_n) \equiv \mathbf{v}_n\}$ along particle trajectories can be approximated as a Markov process if the transition matrix satisfies the Chapman-Kolmogorov equation [e.g., 62], which in matrix form reads as

$$T_n(i, \theta | j, \theta') = \sum_{i', \theta''} T_{n-m}(i, \theta | i', \theta'') T_m(i', \theta'' | j, \theta'). \quad (13)$$

For a Markov process, the m -step transition matrix \mathbf{T}_m is equal to the m -fold product of the

297 1-step transition matrix \mathbf{T}_1 with itself as $\mathbf{T}_m = \mathbf{T}^m$. Recent studies have shown that the spatial
 298 Markov model accurately predicts the transition probabilities, as well as the return probability for
 299 any number of steps [45, 51]. Therefore, a CTRW characterized by a Markov velocity process *in*
 300 *space* is a good approximation for describing average transport.

301 The average particle movements on the random network can be described by the following
 302 system of equations

$$\mathbf{x}_{n+1} = \mathbf{x}_n + l \frac{\mathbf{v}_n}{|\mathbf{v}_n|}, \quad t_{n+1} = t_n + \frac{l}{|\mathbf{v}_n|}. \quad (14)$$

303 The series of Lagrangian velocities $\{\mathbf{v}_n\}_{n=0}^\infty$ is a spatial Markov process and thus fully char-
 304 acterized by the stationary velocity density $p_s(\mathbf{v})$ and the one-step transition PDF $r_1(\mathbf{v}|\mathbf{v}') =$
 305 $\langle \delta(\mathbf{v} - \mathbf{v}_{n+1}) \rangle|_{\mathbf{v}_n=\mathbf{v}'}$. The particle density for the correlated CTRW (14) can be written as

$$P(\mathbf{x}, t) = \int d\mathbf{v} \langle \delta(\mathbf{x} - \mathbf{x}_{n_t}) \delta(\mathbf{v} - \mathbf{v}_{n_t}) \rangle, \quad (15)$$

306 in which $n_t = \max(n | t_n \leq t)$, \mathbf{x}_{n_t} is the position of the node at which the particle is at time t ,
 307 and \mathbf{v}_{n_t} is the velocity by which the particle emanates from this node. The angular brackets denote
 308 here the average over all realization of the stochastic velocity time series $\{\mathbf{v}_n\}$. Equation (15) can
 309 be recast as

$$P(\mathbf{x}, t) = \int d\mathbf{v} \int_{t-l/|\mathbf{v}|}^t dt' R(\mathbf{x}, \mathbf{v}, t'), \quad (16a)$$

in which we defined

$$R(\mathbf{x}, \mathbf{v}, t') = \sum_{n=0}^{\infty} \langle \delta(\mathbf{x} - \mathbf{x}_n) \delta(\mathbf{v} - \mathbf{v}_n) \delta(t' - t_n) \rangle. \quad (16b)$$

The latter satisfies the Kolmogorov type equation

$$R(\mathbf{x}, \mathbf{v}, t) = \delta(\mathbf{x}) p_0(\mathbf{v}) \delta(t) + \int d\mathbf{v}' r_1(\mathbf{v}|\mathbf{v}') \int d\mathbf{x}' \delta(\mathbf{x} - \mathbf{x}' - l\mathbf{v}'/|\mathbf{v}'|) R(\mathbf{x}', \mathbf{v}', t - l/|\mathbf{v}'|), \quad (16c)$$

310 where $p_0(\mathbf{v})$ denotes the distribution of initial particle velocities at step 0. For the injection con-
 311 dition applied here, the initial velocities are sampled uniformly among the network realizations.
 312 Thus, $p_0(\mathbf{v})$ is not equal to the stationary velocity PDF $p_s(\mathbf{v})$, which is obtained by sampling the

velocities equidistantly along a particle path, as outlined above. The correlated CTRW model (16) describes the evolution from an initial PDF $p_0(\mathbf{v})$ towards the steady state PDF through the transition matrix $r_1(\mathbf{v}|\mathbf{v}')$.

For independent successive velocities, i.e., $r_1(\mathbf{v}|\mathbf{v}') = p(\mathbf{v})$, one recovers the CTRW model [e.g., 41]

$$P(\mathbf{x}, t) = \int_0^t dt' R(\mathbf{x}, t') \int_{t-t'}^\infty d\tau \int d\mathbf{x} \psi(\mathbf{x}, \tau), \quad (17a)$$

where $R(\mathbf{x}, t)$ satisfies

$$R(\mathbf{x}, t) = \delta(\mathbf{x})\delta(t) + \int d\mathbf{x}' \int_0^t dt' R(\mathbf{x}', t') \psi(\mathbf{x} - \mathbf{x}', t - t'), \quad (17b)$$

and the joint transition length and time density is given by

$$\psi(\mathbf{x}, t) = \int d\mathbf{v}' p(\mathbf{v}') \delta(\mathbf{x} - l\mathbf{v}'/|\mathbf{v}'|) \delta(t - l/|\mathbf{v}'|). \quad (17c)$$

In the following, we refer to system (16) as *correlated* CTRW because subsequent particle velocities are correlated in space, and to model (17) as *uncorrelated* CTRW because subsequent particle velocities are uncorrelated in space.

Based on the Markovianity assumption of particle transitions, the developed correlated CTRW model is applied to study particle transport in the random network. We compare the results obtained from direct Monte Carlo simulations to both the correlated and uncorrelated CTRW models. Correlated CTRW is characterized by the one-step transition matrix \mathbf{T}_1 determined from numerical Monte Carlo simulations [Figures 10 and 11]. Uncorrelated CTRW is characterized by the Lagrangian velocity distribution $p(\mathbf{v})$, which is obtained from Monte Carlo simulations as well.

The predictions of the developed correlated CTRW model show an excellent agreement with the Monte Carlo simulations for all levels of heterogeneity and mixing rules under consideration [Figures 12, 13(a)(b)(c), and 14(a)]. Note that the direct Monte Carlo simulations are performed by solving Equation (3) in 100 realizations for different mixing rules. Correlated CTRW captures the time evolution of the particle plume with remarkable accuracy, including spatial moments, first passage time distributions and distributions of transverse particle breakthrough positions. Figure 12 shows the time evolution of the longitudinal and transverse MSDs. Both the scaling and the magnitude of the longitudinal spreading are captured accurately by the correlated CTRW model. The model also reproduces accurately the magnitude and evolution of the transverse MSD.

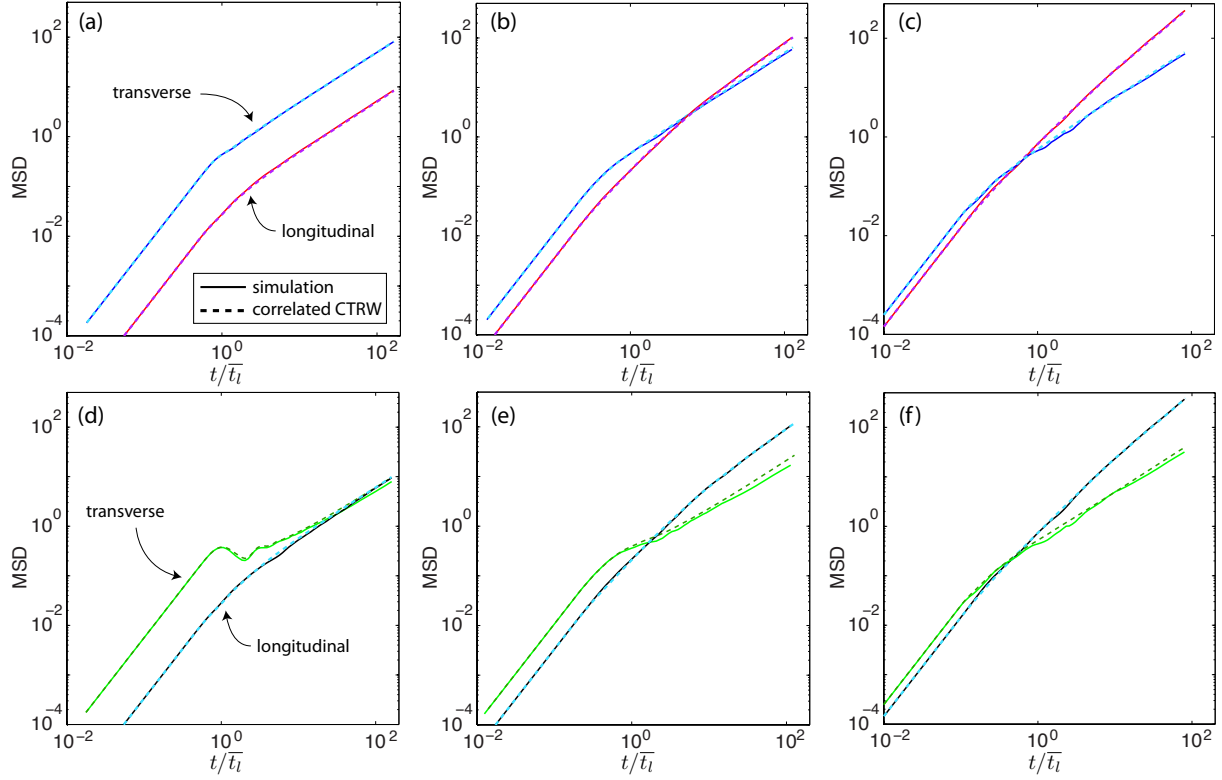


FIG. 12. Time evolution of MSDs obtained from Monte Carlo simulations (solid lines), and the model predictions from the correlated CTRW model (dashed lines). The developed correlated CTRW model is able to accurately capture the time evolution of the MSDs for all levels of heterogeneity strength and mixing rules. (a) $\sigma_{\ln K}^2 = 0.1$, (b) $\sigma_{\ln K}^2 = 1$, and, (c) $\sigma_{\ln K}^2 = 5$ with *complete mixing*, where red line is longitudinal direction and blue line is transverse direction. (d) $\sigma_{\ln K}^2 = 0.1$, (e) $\sigma_{\ln K}^2 = 1$, (f) $\sigma_{\ln K}^2 = 5$ with *streamline routing*, where black line is longitudinal and green line is transverse direction.

Ignoring the correlated structure of the Lagrangian velocity leads to predictions of longitudinal and transverse spreading that deviate from the direct Monte Carlo simulation [Figures 13(d)(e)(f), and 14(b)]. The uncorrelated CTRW model is not able to predict transverse spreading for the streamline routing case [Figure 13(d)(e)(f)], or the peak arrival time and spread of the FPTD [Figures 14(b)]. In contrast, these behaviors are accurately captured by the correlated model.

VI. PARAMETERIZATION OF THE CORRELATED CTRW MODEL

In the previous section, we showed that the effective particle movement can be described by a CTRW whose particle velocities, or transition times, form a spatial Markov process. The latter

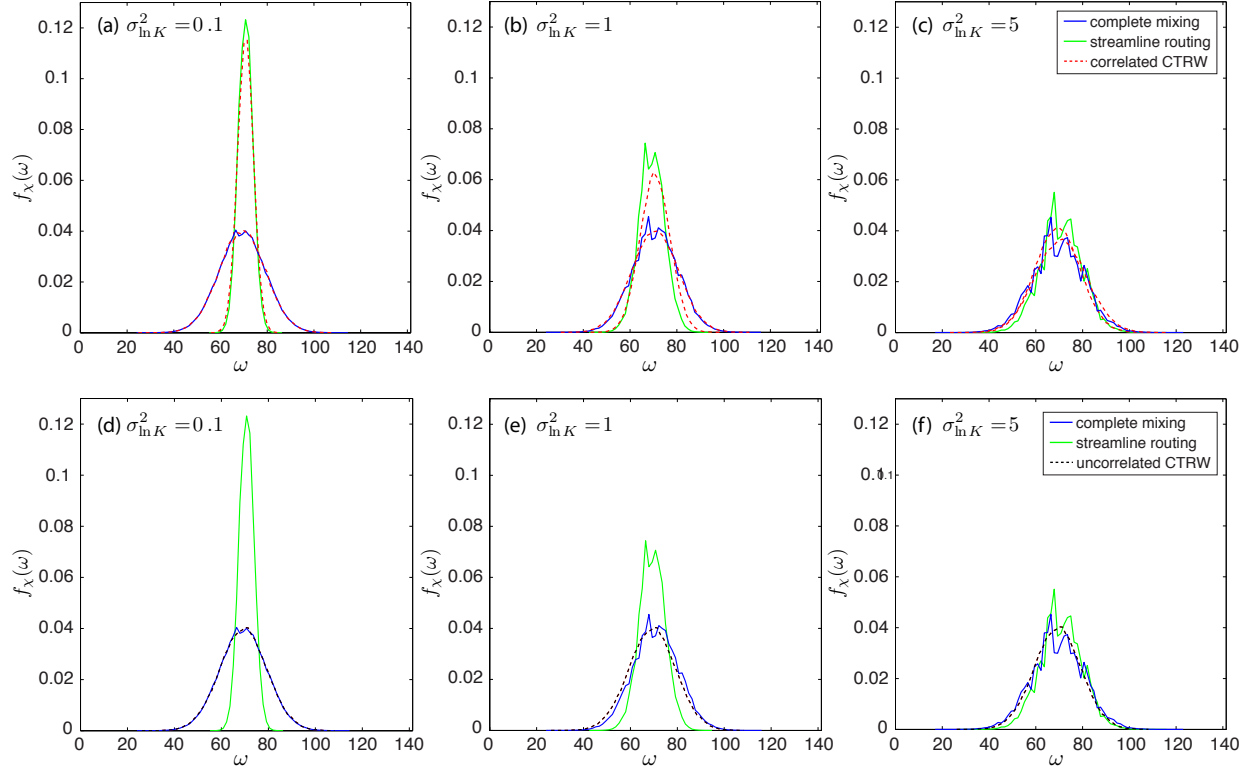


FIG. 13. Probability distributions of transverse particle breakthrough position for Monte Carlo simulations and model predictions. (a) Correlated CTRW for $\sigma_{\ln K}^2 = 0.1$. (b) Correlated CTRW for $\sigma_{\ln K}^2 = 1$. (c) Correlated CTRW for $\sigma_{\ln K}^2 = 5$. (d) Uncorrelated CTRW for $\sigma_{\ln K}^2 = 0.1$. (e) Uncorrelated CTRW for $\sigma_{\ln K}^2 = 1$. (f) Uncorrelated CTRW for $\sigma_{\ln K}^2 = 5$. Uncorrelated CTRW does not have a capability of distinguishing complete mixing and streamline routing cases.

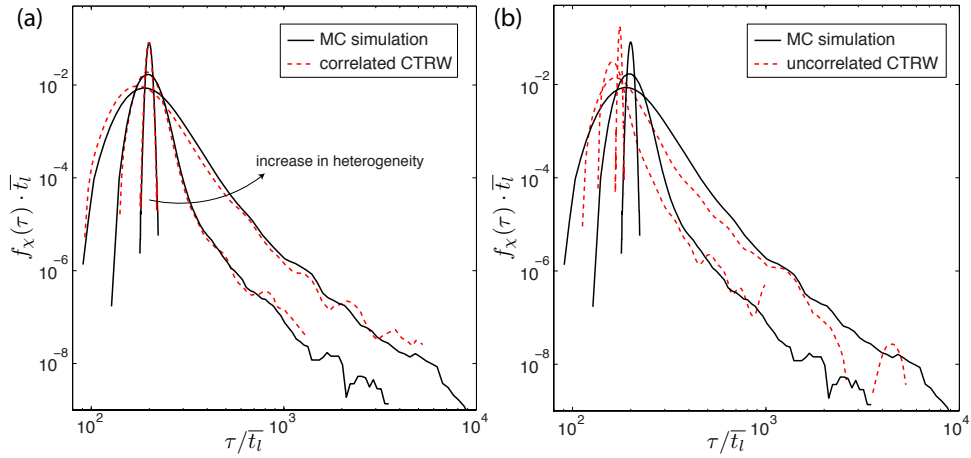


FIG. 14. Particle breakthrough curves from Monte Carlo simulations and model predictions from (a) correlated CTRW, and (b) uncorrelated CTRW.

has been characterized by a velocity transition PDF which has been sampled from the simulated particle velocities. While the resulting correlated CTRW describes the observed behavior well, the application of the approach to experimental data (such as tracer tests) asks for a process model that requires only a few parameters which may be estimated from the available data. Thus, here we consider an explicit Markov process model for subsequent transition times that captures the essential features of correlation with a minimal set of parameters. To accomplish this, we follow the approach of [18], who recently proposed an effective parameterization of the correlated CTRW model and applied it to the interpretation of field-scale tracer transport experiments.

We consider the series of streamwise particle velocities $v_n = |\mathbf{v}_L(s_n)|$ and model them as a Markov process $\{v_n\}$ through the steady state velocity PDF, $\psi_v(v)$, and the transition matrix \mathbf{T} [63]. First note that v is discretized into N classes, $v \in \bigcup_{i=1}^N (v_{c,i}, v_{c,i+1}]$, such that the transition probabilities between the classes are represented by the $N \times N$ transition matrix \mathbf{T} . Here, we choose equiprobable binning such that the class limits $v_{c,i}$ are given implicitly by

$$\int_{v_{c,i}}^{v_{c,i+1}} dt \psi_\tau(t) = \frac{1}{N}. \quad (18)$$

With this condition, \mathbf{T} is a doubly stochastic matrix, which satisfies $\sum_{i=1}^N T_{ij} = \sum_{j=1}^N T_{ij} = 1$. For a large number of transitions it converges towards uniformity

$$\lim_{n \rightarrow \infty} [\mathbf{T}^n]_{ij} = \frac{1}{N}, \quad (19)$$

whose eigenvalues are 1 and 0. Correlation is measured by the convergence of \mathbf{T} towards the uniform matrix. The characteristic number of steps over which the Markov chain is correlated, is determined by the decay rate of the second largest eigenvalue χ_2 of \mathbf{T} (the largest eigenvalue of a stochastic matrix is always 1). The convergence towards uniformity can be quantified by the correlation function $C(n) = \chi_2^n$, which can be written as

$$C(n) = \exp\left(-\frac{n}{n_c}\right), \quad n_c = -\frac{1}{\ln(|\chi_2|)}. \quad (20)$$

The transition matrix is characterized by n_c , which determines the characteristic number of steps for convergence towards uniformity. Thus, we consider here a Markov model whose transition matrix is characterized by just two eigenvalues, namely 1 and χ_2 . Its transition matrix is given by

$$T_{ij} = a\delta_{ij} + (1 - a)\frac{1 - \delta_{ij}}{N - 1}. \quad (21)$$

It describes a Markov process that remains in the same state with probability a and changes to a different state, whose distribution is uniform, with probability $1 - a$. The diagonal value of $a \leq 1$ determines the correlation strength. A value of $a = 1$ implies perfect correlation, which renders the N -dimensional unity matrix, $T_{ij} = \delta_{ij}$. For $a = 1/N$, all transitions are equally probable, and the transition matrix is equal to the uniform matrix with $T_{ij} = 1/N$. The eigenvalues of the transition matrix (21) are $\chi_1 = 1$ and

$$\chi_2 = \frac{Na - 1}{N - 1}. \quad (22)$$

Thus, the number n_c of correlation steps is given by

$$n_c = -\frac{1}{\ln\left(\frac{Na-1}{N-1}\right)} \stackrel{N \gg 1}{\approx} -\frac{1}{\ln(a)}. \quad (23)$$

It is uniquely determined by the value of a . The value of a can be estimated from the correlation function $\chi_s(s)$ of streamwise Lagrangian velocity given by Equation (8). The streamwise velocity correlation function is given in terms of the velocity time series $\{v_n\}$ as

$$\chi(s_{n+m} - s_n) = \frac{\langle v'_{n+m} v'_n \rangle}{\langle v'^2_n \rangle}, \quad (24)$$

where we defined $v'_n = v_n - \langle v \rangle$ with $\langle v \rangle$ the mean streamwise velocity and $s_n = nl$. Using the discretization (18) of streamwise velocities into N equiprobable bins and the transition matrix \mathbf{T} , the velocity correlation can be written as

$$\chi_s(s_{n+m} - s_n) = \frac{\frac{1}{N} \sum_{i,j=1}^N v'_{c,i} [\mathbf{T}^m]_{ij} v'_{c,j}}{\frac{1}{N} \sum_{i=1}^N v'^2_{c,i}}. \quad (25)$$

Note that the transition matrix \mathbf{T} given by (21) is symmetric and has only the two eigenvalues, $\chi_1 = 1$ and χ_2 given by (22) with χ_2 of order $N - 1$. Thus, performing a base transformation in (25) into the eigensystem of \mathbf{T} , one sees that

$$\chi_s(s_{n+m} - s_n) = \exp\left(-\frac{|s_{n+m} - s_n|}{\ell_c}\right), \quad (26)$$

where the correlation length is given by $\ell_c = n_c l$. Thus, n_c is directly related to the correlation length of the streamwise Lagrangian velocity. Note that $\ell_c = 0$ for zero correlation and $\ell_c = \infty$ for perfect correlation. As illustrated in Figure 8(b), $\chi_s(s)$ is well approximated by an exponential function. Thus, we obtain a from the correlation length ℓ_c as $a = \exp(-l/\ell_c)$. The transition matrix \mathbf{T} is fully parameterized in terms of the correlation length of the streamwise Lagrangian velocity.

To describe the observed steady state velocity distribution $\psi_v(v)$ we consider the equivalent distribution $\psi_\tau(\tau)$ of transition times $\tau = l/v$, which is illustrated in Figure 8(a). It is well described by the following truncated power-law distribution

$$\psi_\tau(t) \sim \frac{\exp(-\tau_0/t)}{(t/\tau_0)^{1+\beta}}, \quad (27)$$

where τ_0 determines the early time cutoff, and β the power-law slope. Note that τ_0 and β are both positive coefficients. The slope β of the power-law regime describes the heterogeneity of the velocity distribution. As β decreases, the transport becomes more anomalous because the probability of experiencing large transition times increases. Therefore, smaller β can be understood to represent higher flow heterogeneity, as is well known in the CTRW modeling framework [43]. Indeed, the estimated β values decrease as the conductivity distribution becomes more heterogeneous (we obtain $\beta = 18, 2.6, 1.7$ for $\sigma_{\ln K}^2 = 0.1, 1, 5$, respectively). We estimate the parameters τ_0 and β from the measured transition time distributions [Figure 8(a)]. As pointed out recently by [64], the tail behavior of the transition time PDF as quantified by the exponent β may in principle be related to the lower end of the distribution of hydraulic conductivity.

The velocity PDF is obtained from the transition time PDF by $\psi_v(v) = (l/v^2)\psi_\tau(l/v)$ and quantifies together with the transition matrix \mathbf{T} the velocity heterogeneity and velocity correlation structure. To honor the network geometry and to accurately estimate transverse spreading we need one more input parameter that quantifies the velocity directionality. Since the majority of velocity transitions are forward-forward, we only consider E, M, G and O transitions. We need a additional parameter that quantifies the probability of changing (either M or G) or maintaining the direction (either E or O), and define γ as the probability of changing and $1 - \gamma$ is the probability of maintaining the direction. The measured γ values for the complete mixing rule are in all cases ~ 0.5 ,

independently of conductivity distributions. This is because the complete mixing rule maximizes transverse excursions. However, for streamline routing γ is very sensitive to the underlying conductivity distribution. It decreases as the conductivity distribution becomes more heterogeneous (we find $\gamma = 0.89, 0.71, 0.58$ for $\sigma_{\ln K}^2 = 0.1, 1, 5$, respectively). This is because the probability of transitioning to an adjacent link is higher for the streamline routing case, and as the conductivity heterogeneity increases the probability of transitioning to the opposite link increases.

In summary, the correlated CTRW model for the random network under consideration is characterized by four independent parameters that determine the velocity distribution and the velocity correlation structure: β , which characterizes the slope of the truncated power-law distribution; τ_0 , which characterizes the early time cutoff of the transition time distribution; a , which quantifies the velocity correlation; and γ , which quantifies the velocity transition directionality.

In order to test the predictive power of the parametric correlated CTRW model, the model predictions are compared to the results obtained from the direct Monte Carlo simulations. We obtain an excellent agreement with the Monte Carlo results for all the conductivity distributions and mixing rules that we studied (Figures 15 and 16). The model accurately captures the time evolution of the particle plumes, including spatial moments, first passage time distributions and the distributions of the transverse particle breakthrough positions (Figures 15 and 16).

The fact that the parametric correlated CTRW proves as good here as the more complex correlated CTRW model presented in the previous section is noteworthy, as the parametric model involves only four parameters. In particular, the previous CTRW model quantifies explicitly the transition probability of each velocity class to the others, while the parametric correlated CTRW model only quantifies the probability to stay in the same velocity class and it assumes that the probability to jump to any other class is independent of velocity. This assumption is likely valid here since there is nearly no dependence of the velocity correlation properties on the velocity (Figure 11). This assumption would break down in systems where transitions from one velocity to the other is strongly dependent on velocity. For instance, in highly channelized systems, the probability for particles to stay in high velocity channels may be different from their probability to stay in low velocity areas (see discussion in [65]). This result represents an important step towards the application of this framework to the field. As discussed in [18], the model parameters can be estimated by analyzing jointly cross-borehole and push-pull tracer tests. In particular, velocity correlation is key to distinguishing reversible from irreversible dispersion, which is linked to the difference between spreading and mixing.

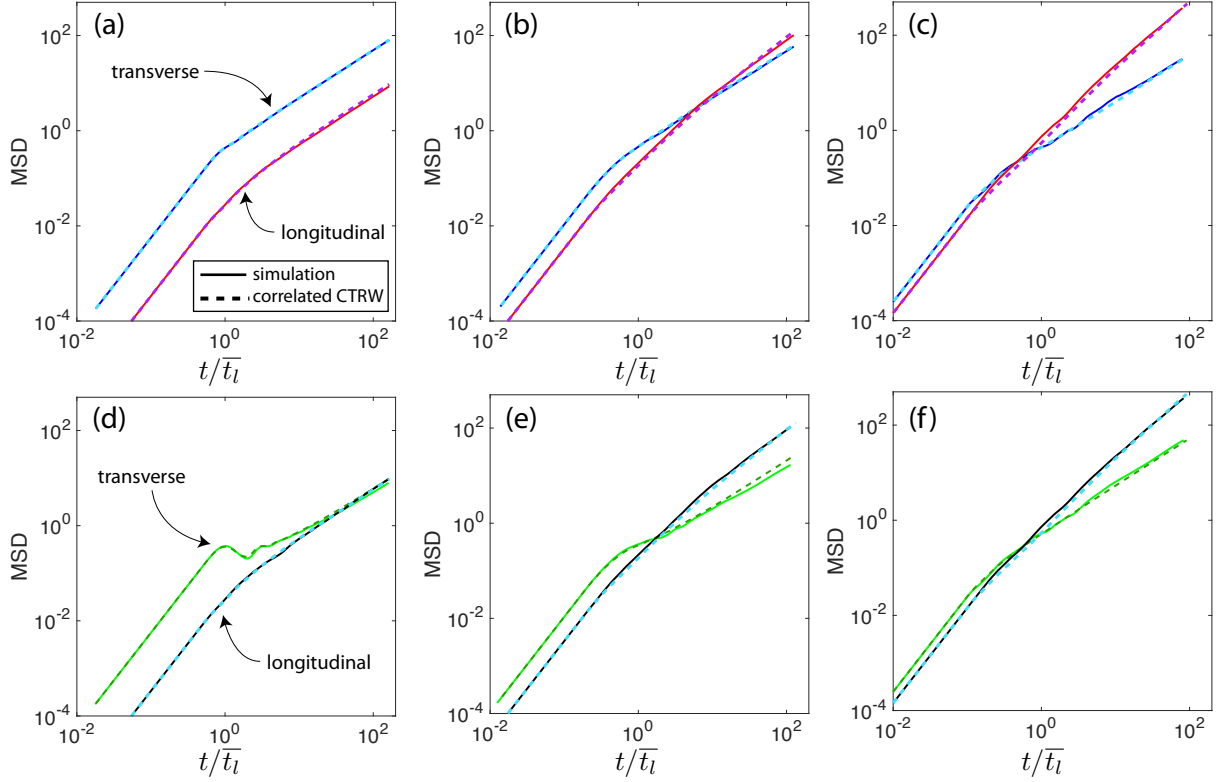


FIG. 15. Comparison between the time evolution of the MSDs obtained from the Monte Carlo simulations (solid lines) and the model predictions from the *parametric* correlated CTRW model (dashed lines). The proposed model is able to accurately capture the time evolution of the MSDs for all levels of heterogeneity and mixing rules under consideration. (a) $\sigma_{\ln K}^2 = 0.1$, (b) $\sigma_{\ln K}^2 = 1$, (c) $\sigma_{\ln K}^2 = 5$ with *complete mixing*, where red line is longitudinal direction and blue line is transverse direction. (d) $\sigma_{\ln K}^2 = 0.1$, (e) $\sigma_{\ln K}^2 = 1$, (f) $\sigma_{\ln K}^2 = 5$ with *streamline routing*, where black line is longitudinal and green line is transverse direction.

VII. CONCLUSIONS

Fracture networks characterized by conductivity heterogeneity and different mixing rules at fracture intersections lead to non-trivial transport behavior often characterized by non-Fickian dispersion properties in both longitudinal and transverse directions. The divergence-free condition arising from mass conservation leads to a correlated flow field with preferential paths, even when the underlying conductivity field is completely uncorrelated. Mixing rules at nodes are shown to have a major impact on transverse mixing. In particular, the streamline routing rule leads to subdiffusive transverse spreading behavior. While velocity distributions are mainly controlled by the underlying conductivity distributions, the velocity correlation structure is determined by the

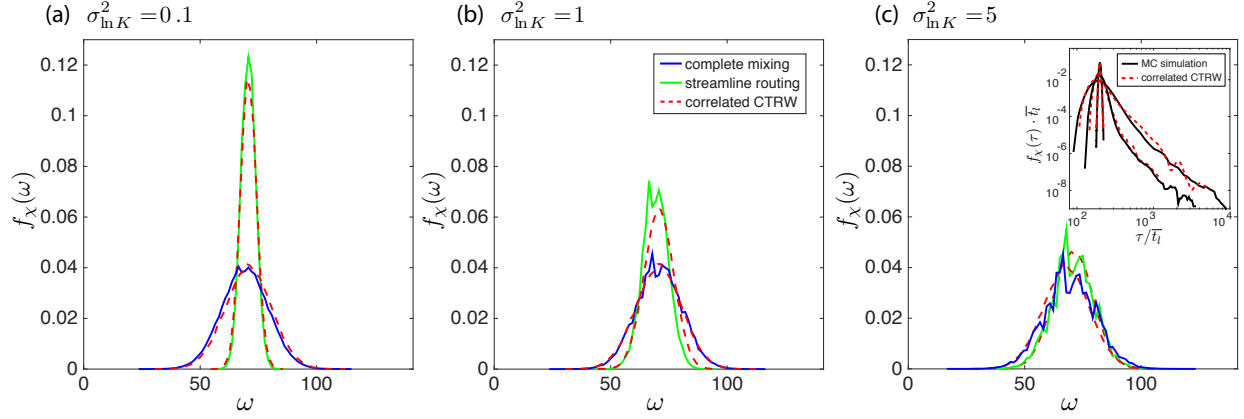


FIG. 16. Probability distributions of the transverse particle breakthrough positions obtained from Monte Carlo simulations, and predictions from the parametric correlated CTRW model. (a) $\sigma_{\ln K}^2 = 0.1$. (b) $\sigma_{\ln K}^2 = 1$. (c) $\sigma_{\ln K}^2 = 5$. Inset: Particle breakthrough curves from Monte Carlo simulations and model predictions from the parametric correlated CTRW model.

interplay between network heterogeneity and mixing rule at nodes.

Here, we propose and validate a spatial Markov model that is fully parameterized from the velocity field distribution and spatial correlation properties, and explicitly captures the multidimensional effects associated with changes in direction along the particle trajectory. In particular, we discuss the impact of spatial velocity correlations, which are typically not included in the classical CTRW framework, on the transport behavior. To make this model amenable to field applications, we develop a parametric model formulation containing a minimum set of parameters that still captures the main properties of the velocity field relevant for transport: β characterizes the slope of the truncated power-law velocity distribution, τ_0 characterizes the early time cutoff of the transition time distribution, a quantifies the velocity correlation, and γ quantifies the velocity transition directionality.

The excellent agreement between the model and the numerical simulations provides a validation of this parametric correlated CTRW approach, whose parameters can be determined from field tracer tests [18] to assess the respective role of velocity distributions and velocity correlations *in situ*. It is important to note that, in its current formulation, the parametric correlated CTRW model assumes an identical correlation length over all velocity classes. This assumption allows us to quantify velocity correlation with a single parameter, but could be an oversimplified approach for certain cases. For example, correlated conductivity field with strong preferential paths may lead

to longer velocity correlation length for high velocities compared to small velocities. This should be investigated in future research and we conjecture that assigning variable correlation length as a function of velocity class could be a promising approach.

Finally, our study shows how the interplay between fracture geometrical properties (conductivity distribution and network geometry) and physical transport mechanisms (the balance between advection and diffusion that determines mixing at the fracture scale) controls average particle transport via Lagrangian velocity statistics. We conjecture that the proposed correlated CTRW model may provide an avenue to link the model parameters to geometrical and physical transport mechanisms.

ACKNOWLEDGMENTS

RJ acknowledges the support of the US Department of Energy (grant DE-SC0003907), and a MISTI Global Seed Funds award. MD acknowledges the support of the European Research Council (ERC) through the project MHetScale (617511). TLB acknowledges the support of the INTERREG IV project CLIMAWAT.

-
- [1] G. S. Bodvarsson, W. B., R. Patterson, and D. Williams, J. Contaminant Hydrol. **38**, 3 (1999).
 - [2] K. Pruess, Geothermics **35**, 351 (2006).
 - [3] A. Rinaldo *et al.*, Proc. Natl. Acad. Sci. USA **109**, 6602 (2012).
 - [4] G. M. Whitesides, Nature **442**, 368 (2006).
 - [5] B. S. Kerner, Phys. Rev. Lett. **81**, 3797 (1998).
 - [6] J. D. Seymour, J. P. Gage, S. L. Codd, and R. Gerlach, Phys. Rev. Lett. **93**, 198103 (2004).
 - [7] U. M. Scheven, D. Verganelakis, R. Harris, M. L. Johns, and L. F. Gladden, Phys. Fluids **17**, 117107 (2005).
 - [8] B. Bijeljic, P. Mostaghimi, and M. J. Blunt, Phys. Rev. Lett. **107**, 204502 (2011).
 - [9] P. K. Kang, P. de Anna, J. P. Nunes, B. Bijeljic, M. J. Blunt, and R. Juanes, Geophys. Res. Lett. **41**, 6184 (2014).
 - [10] Y. Hatano and N. Hatano, Water Resour. Res. **34**, 1027 (1998).
 - [11] A. Cortis and B. Berkowitz, Soil Sci. Soc. Am. J. **27**, 1539 (2004).

- 497 [12] P. Heidari and L. Li, *Water Resour. Res.* **50**, 8240 (2014).
- 498 [13] S. P. Garabedian, D. R. LeBlanc, L. W. Gelhar, and M. A. Celia, *Water Resour. Res.* **27**, 911 (1991).
- 499 [14] M. W. Becker and A. M. Shapiro, *Water Resour. Res.* **36**, 1677 (2000).
- 500 [15] R. Haggerty, S. W. Fleming, L. C. Meigs, and S. A. McKenna, *Water Resour. Res.* **37**, 1129 (2001).
- 501 [16] S. A. McKenna, L. C. Meigs, and R. Haggerty, *Water Resour. Res.* **37**, 1143 (2001).
- 502 [17] T. Le Borgne and P. Gouze, *Water Resour. Res.* **44**, W06427 (2008).
- 503 [18] P. K. Kang, T. Le Borgne, M. Dentz, O. Bour, and R. Juanes, *Water Resour. Res.* **51**, 940 (2015).
- 504 [19] I. Golding and E. C. Cox, *Phys. Rev. Lett.* **96**, 098102 (2006).
- 505 [20] P. Massignan, C. Manzo, J. A. Torreno-Pina, M. F. García-Parajo, M. Lewenstein, and G. J. Lapeyre
506 Jr., *Phys. Rev. Lett.* **112**, 150603 (2014).
- 507 [21] G. M. Viswanathan, V. Afanasyev, S. V. Buldyrev, E. J. Murphy, P. A. Prince, and H. E. Stanley,
508 *Nature* **381**, 413 (1996).
- 509 [22] M. F. Shlesinger, *J. Stat. Phys.* **10**, 421 (1974).
- 510 [23] J. P. Bouchaud and A. Georges, *Phys. Rep.* **195**, 127 (1990).
- 511 [24] R. Metzler and J. Klafter, *Phys. Rep.* **339**, 1 (2000).
- 512 [25] J. Molinero and J. Samper, *J. Contaminant Hydrol.* **82**, 293 (2006).
- 513 [26] N. Yoshida and Y. Takahashi, *Elements* **8**, 201 (2012).
- 514 [27] E. Abarca, E. Vazquez-Sune, J. Carrera, B. Capino, D. Gamez, and F. Batlle, *Water Resour. Res.* **42**,
515 W09415 (2006).
- 516 [28] S. L. Culkin, K. Singha, and F. D. Day-Lewis, *Groundwater* **46**, 591 (2008).
- 517 [29] J. Regnery, J. Lee, P. Kitanidis, T. Illangasekare, J. O. Sharp, and J. E. Drewes, *Environ. Eng. Sci.* **30**,
518 409 (2013).
- 519 [30] B. Berkowitz and H. Scher, *Phys. Rev. Lett.* **79**, 4038 (1997).
- 520 [31] M. Dentz, A. Cortis, H. Scher, and B. Berkowitz, *Adv. Water Resour.* **27**, 155 (2004).
- 521 [32] S. Geiger, A. Cortis, and J. T. Birkholzer, *Water Resour. Res.* **46**, W12530 (2010).
- 522 [33] L. Wang and M. B. Cardenas, *Water Resour. Res.* **50**, 871 (2014).
- 523 [34] M. Dentz, P. K. Kang, and T. Le Borgne, *Adv. Water Resour.* **82**, 16 (2015).
- 524 [35] J. H. Cushman and T. R. Ginn, *Water Resour. Res.* **36**, 3763 (2000).
- 525 [36] D. A. Benson, S. W. Wheatcraft, and M. M. Meerschaert, *Water Resour. Res.* **36**, 1403 (2000).
- 526 [37] R. Haggerty and S. M. Gorelick, *Water Resour. Res.* **31**, 2383 (1995).
- 527 [38] J. Carrera, X. Sánchez-Vila, I. Benet, A. Medina, G. A. Galarza, and J. Guimerá, *Hydrogeol. J.* **6**, 178

(1998).

[39] M. W. Becker and A. M. Shapiro, Water Resour. Res. **39**, 1024 (2003).

[40] R. Benke and S. Painter, Water Resour. Res. **39**, 1324 (2003).

[41] H. Scher and E. W. Montroll, Phys. Rev. B **12**, 2455 (1975).

[42] J. Klafter and R. Silbey, Phys. Rev. Lett. **44**, 55 (1980).

[43] B. Berkowitz, A. Cortis, M. Dentz, and H. Scher, Rev. Geophys. **44**, RG2003 (2006).

[44] C. Nicolaides, L. Cueto-Felgueroso, and R. Juanes, Phys. Rev. E **82**, 055101(R) (2010).

[45] T. Le Borgne, M. Dentz, and J. Carrera, Phys. Rev. Lett. **101**, 090601 (2008).

[46] M. Dentz and A. Castro, Geophys. Res. Lett. **36**, L03403 (2009).

[47] M. Dentz and D. Bolster, Phys. Rev. Lett. **105**, 244301 (2010).

[48] P. K. Kang, M. Dentz, and R. Juanes, Phys. Rev. E **83**, 030101(R), doi:10.1103/PhysRevE.83.030101 (2011).

[49] B. Berkowitz and H. Scher, Phys. Rev. E **81**, 011128 (2010).

[50] D. W. Meyer and H. A. Tchelepi, Water Resour. Res. **46**, W11552 (2010).

[51] P. K. Kang, M. Dentz, T. Le Borgne, and R. Juanes, Phys. Rev. Lett. **107**, 180602, doi:10.1103/PhysRevLett.107.180602 (2011).

[52] P. de Anna, T. Le Borgne, M. Dentz, A. M. Tartakovsky, D. Bolster, and P. Davy, Phys. Rev. Lett. **110**, 184502 (2013).

[53] S. S. Datta, H. Chiang, T. S. Ramakrishnan, and D. A. Weitz, Phys. Rev. Lett. **111**, 064501 (2013).

[54] S. Painter and V. Cvetkovic, Water Resour. Res. **41**, W02002 (2005).

[55] B. Dverstorp, J. Andersson, and W. Nordqvist, Water Resour. Res. **28**, 2327 (1992).

[56] B. Berkowitz, C. Naumann, and L. Smith, Water Resour. Res. **30**, 1765 (1994).

[57] H. W. Stockman, C. Li, and J. L. Wilson, Geophys. Res. Lett. **24**, 1515 (1997).

[58] Y. J. Park, J. Dreuzy, K. K. Lee, and B. Berkowitz, Water Resour. Res. **37**, 2493 (2001).

[59] J. Bear, *Dynamics of Fluids in Porous Media* (Elsevier, New York, 1972).

[60] X. Sanchez-Vila, A. Guadagnini, and J. Carrera, Rev. Geophys. **44**, RG3002 (2006).

[61] R. A. Freeze and J. A. Cherry, *Groundwater* (Prentice-Hall, 1977).

[62] H. Risken, *The Fokker–Planck Equation*, 2nd ed. (Springer, Berlin, 1989).

[63] M. A. Pinsky and S. Karlin, *An introduction to stochastic modeling* (Academic press, 2010).

[64] Y. Edery, A. Guadagnini, H. Scher, and B. Berkowitz, Water Resour. Res. **50**, doi:10.1002/2013WR015111 (2014).

559 [65] T. Le Borgne, M. Dentz, and J. Carrera, Phys. Rev. E **78**, 026308 (2008).